Thin Solid Films 646 (2018) 180–189

Contents lists available at ScienceDirect

Thin Solid Films

journal homepage: www.elsevier.com/locate/tsf

Solution processed $CuSbS_2$ films for solar cell applications

Michael E. Edley, Borirak Opasanont, Jason T. Conley, Hoang Tran, Sergey Y. Smolin, Siming Li, Andrew D. Dillon, Aaron T. Fafarman, Jason B. Baxter*

Department of Chemical and Biological Engineering, Drexel University, Philadelphia, PA 19104, USA

ARTICLE INFO

Keywords:
Nanocrystal
Copper antimony sulfide
Electrophoretic deposition
Ligand exchange
Terahertz spectroscopy

ABSTRACT

$CuSbS_2$ is a semiconductor with a band gap of 1.5 eV and earth-abundant constituent elements, indicating potential promise as a photovoltaic absorber material. However, strategies to fabricate $CuSbS_2$ films, especially using solution processing, have not been thoroughly developed. We report on two solution-based approaches to deposit $CuSbS_2$ films: chemical bath deposition (CBD) and deposition of colloidal nanoplates. Conditions to directly deposit ternary $CuSbS_2$ (chalcostibite) films were not found, but $CuSbS_2$ films could be formed by annealing CBD-grown bilayers of CuS and Sb_2S_3. Simultaneous control over phase purity and film morphology proved elusive. To address this challenge, we synthesized colloidal nanoplates of phase-pure chalcostibite $CuSbS_2$ capped with oleylamine ligands following a literature procedure. When colloids are condensed into thin films, these synthesis ligands are insulating and inhibit the inter-crystal charge transfer that is necessary for long-range charge transport. To solve this problem, two approaches were pursued: convective assembly followed by solid-state ligand exchange and a novel process involving solution-phase ligand exchange followed by electrophoretic deposition (EPD). Replacement of oleylamine with S^{2-} increased the film conductivity by two orders of magnitude. S^{2-} capping groups also increased the electrophoretic mobility and enabled EPD at bias voltages as low as 5 V. Time-resolved terahertz spectroscopy indicated transient photoconductivity persisting beyond 1 ns and carrier mobilities of $\sim 1\ cm^2\ V^{-1}\ s^{-1}$. While many challenges remain, this work indicates the potential promise of solution-processed $CuSbS_2$ nanoplates as building blocks for photovoltaic devices.

1. Introduction

Photovoltaics can provide a clean and renewable source of electricity, and much current research focuses on reducing cost and improving scalability through development of efficient thin film technologies that utilize earth-abundant materials. Several copper-containing materials have shown particular promise as thin film absorbers. $CuIn_xGa_{(1-x)}Se_2$ (CIGS) has been heavily researched for several decades and has achieved cell efficiencies of 22.6% [1]. However, indium is rare and expensive, which may limit the use of CIGS for power generation at very large scales. $Cu_2ZnSn(S,Se)_4$ (CZTSSe) is being pursued as a more earth-abundant option than CIGS. CZTSSe has benefited from the vast knowledge base on CIGS and attained efficiencies of 12.6% [2]. However, improvements in efficiency have stagnated, partly because of deep traps and band-edge potential fluctuations that are difficult to control due to the complex chemistry of the quaternary/quinary system. Alternatively, $CuSbS_2$ is a ternary compound that has an optimal band gap (1.5–1.6 eV), large absorption coefficient, and non-toxic, earth-abundant constituent elements [3]. Additionally, $CuSbS_2$ has a simpler chemistry than CZTSSe and may be easier to control, while also taking advantage of the extensive knowledge base on CIGS thin film photovoltaics.

$CuSbS_2$ solar cells with efficiencies of 3–4% have utilized films produced by sequential electrodeposition of Cu and Sb metals followed by sulfurization [4], co-sputtering of Sb_2S_3 and Cu_2S [5], or deposition of a hybrid ink with Cu and Sb precursors followed by sulfurization [6]. Losses in the external quantum efficiency at energies above the band gap suggest that solar cell performance was limited by minority carrier diffusion [4]. Diffusion length is proportional to $(\mu\tau)^{1/2}$, where μ is the mobility and τ is the photoexcited carrier lifetime. Carrier lifetimes of 0.7 ns and hole mobility of $4\ cm^2\ V^{-1}\ s^{-1}$ were recently reported for co-sputtered $CuSbS_2$ films [7]. Despite their importance, the literature is otherwise lacking in direct characterization of $CuSbS_2$ carrier dynamics for solar cell applications.

Additionally, there is a scarcity of reports on alternative solution synthesis routes to ternary chalcostibite films [6,8–13]. Large differences in solubilities of Cu and Sb precursors have made single-step synthesis of $CuSbS_2$ thin films via traditional solution-based semiconductor synthesis methods such as chemical bath deposition (CBD) a great challenge. The Nair group introduced a sequential CBD approach

* Corresponding author.
E-mail address: jbaxter@drexel.edu (J.B. Baxter).

https://doi.org/10.1016/j.tsf.2017.12.002
Received 6 June 2017; Received in revised form 27 October 2017; Accepted 4 December 2017
Available online 06 December 2017
0040-6090/ © 2017 Elsevier B.V. All rights reserved.

based on annealing a CuS-Sb_2S_3 bilayer, but morphology of the films was not shown [11]. More recently, films deposited from dissolved precursors (molecular inks) have been reported. Thiol-amine based inks developed by the Brutchey [12] group [9] and hydrazine inks reported by the Tang group resulted in high-quality films, although hydrazine is highly hazardous.

Alternatively, recent advances in quantum dot solar cells provide inspiration for approaches based on casting films of high-purity nanocrystals from colloidal suspensions [14,15]. Highly phase-pure, low mosaicity nanocrystals are readily synthesized in hot organic solvents in the presence of organic surfactants that remain after synthesis as surface capping groups or 'ligands'. Thereafter, such ligands are critical determinants of colloidal stability. However, when the colloids are condensed into thin films these bulky, insulating synthesis ligands inhibit inter-nanocrystal charge transfer. Over the last several years, chemical processes have been developed to exchange the synthesis ligands with shorter ligands, thereby enhancing electronic coupling between nanocrystals and enabling functional films with long-range conductivity [16–22]. While processing and properties of ligand-exchanged cadmium and lead chalcogenide nanocrystals have been heavily investigated [17,19,23–31], extending these ligand exchange chemistries to new materials poses significant challenges; [17] no such studies for $CuSbS_2$ nanoparticles have been reported previously.

In this work, we have used CBD to deposit CuS and Sb_2S_3 binary layers that were annealed to form $CuSbS_2$, but conditions were not found that simultaneously allowed for direct control over phase purity and desirable morphology for solar cell applications. In contrast, direct synthesis of the desired chalcostibite phase in the form of colloidal nanoplates with dimensions of 300 nm by 400 nm by 50 nm was achieved using a modification of hot-injection methods reported previously [32,33]. These colloidal building blocks were then processed into functional films using either convective assembly or electrophoretic deposition (EPD). For both deposition techniques, different chemical approaches were herein optimized to exchange the synthesis ligands with the compact, inorganic ligand S^{2-} [18]. This step is performed either before (EPD) or after (convective assembly) deposition to ultimately render the film conductive. Post-deposition ligand exchange of convectively assembled films increased their conductivity by two orders of magnitude. In colloidal dispersions, the S^{2-} ligand increased the electrophoretic mobility of the nanoplates, allowing for EPD with applied bias of only 5 V, which is a 50 × reduction compared to as-synthesized nanocrystals. Time-resolved terahertz spectroscopy was applied to understand the photoexcited carrier dynamics of the nanoplate films, revealing carrier mobilities of ~1 $cm^2 V^{-1} s^{-1}$ and transient photoconductivity that persisted into the nanosecond range.

2. Materials and methods

2.1. $CuSbS_2$ films from CuS and Sb_2S_3 bilayers

Films were deposited on F:SnO_2-coated glass (FTO, 15 Ω − 2/sq, Hartford Glass), soda-lime glass, and quartz substrates. All substrates were cleaned by successive sonication at 60 °C for 15 min in 20% CONTRAD 70 (Decon Laboratories), 1:1 acetone:ethanol, and 1 M hydrochloric acid. The substrates were then thoroughly washed with DI water and dried with nitrogen gas. A CuS layer and a Sb_2S_3 layer were sequentially deposited on the substrate, followed by thermal annealing to form the ternary thin film. This approach follows the general bilayer concept reported by the Nair group and is described in further detail below [11].

CBD of CuS films followed the procedure reported by Kim et al. [34], with a solution of 80 mM $Na_2S_2O_3$ and 20 mM $CuSO_4$. pH of the solution was adjusted to 2.3 with hydrochloric acid. To generate the deposition bath, $Na_2S_2O_3$ and $CuSO_4$ solutions were prepared individually and heated to a reaction temperature of 70 °C with a water bath. $CuSO_4$ was then vigorously mixed into the $Na_2S_2O_3$ solution and reacted for 3 h at 70 °C, yielding a film thickness of 150 nm on FTO.

Sb_2S_3 films were deposited on top of the CuS by CBD following a recipe adapted from Messina et al. [35] Bright orange-red Sb_2S_3 films were deposited via CBD at 4 °C from an aqueous solution of 28.5 mM $SbCl_3$ and 250 mM $Na_2S_2O_3$. The desired concentrations were achieved from 1.14 M $SbCl_3$ in acetone and 1 M $Na_2S_2O_3$ in water. The $SbCl_3$ solution was vigorously mixed into the $Na_2S_2O_3$ solution and diluted to the desired reaction concentrations with DI water. The vessel was capped for the entire reaction time, typically 4 h, which yielded films that were 250 nm thick.

Ternary $CuSbS_2$ films were fabricated by thermally annealing the Sb_2S_3/CuS bilayers. Thermal annealing was carried out on a hot plate in a N_2-filled glovebox. In some cases, attempts to control Sb and S outgassing were made by reducing the overhead volume with a glass structure, as described below. The limit of zero overhead volume was also investigated by directly contacting a glass substrate to the Sb_2S_3/CuS stack. Typically, a diffusion step at 200 °C for 2 h was followed by a higher temperature step between 300 °C and 400 °C for crystallite growth.

2.2. Mesoporous films from colloidal $CuSbS_2$

2.2.1. Nanoplate synthesis

$CuSbS_2$ nanoplates were synthesized via colloidal hot-injection methods in a Schlenk line following the method reported by Ramasamy et al. [36] 0.50 mmol of $Cu(acac)_2$, 0.50 mmol of $SbCl_3·6H_2O$, and 10 mL of oleylamine (OLA) were degassed for 15 min and then backfilled with nitrogen for 15 min, followed by heating to the reaction temperature of 220 °C. In a second reaction flask, 1.3 mmol of elemental sulfur was dissolved in 1 mL of OLA, then degassed for 5 min and backfilled with nitrogen for 5 min three times. The reaction was initiated by rapidly injecting the sulfur solution into the metal precursor solution. The reaction continued for 10 or 30 min and was then quenched by removing the heat jacket and cooling using a cold air gun. Nanoplates were washed with 15 mL of hexanes and 15 mL of ethanol, then centrifuged at 6000 rpm for 5 min. This process was repeated 3 times. After washing, the nanoplates were typically dispersed in chloroform or hexanes.

2.2.2. Films from convective assembly and solid-state ligand exchange

Convective assembly was used to deposit mesoporous films of $CuSbS_2$ nanoplates on FTO, soda-lime glass, or quartz. In a typical deposition, a 0.4 mg/mL dispersion of $CuSbS_2$ nanoplates in chloroform was added to a vessel containing a substrate mounted at an angle of 30°. As the solvent evaporated, $CuSbS_2$ nanoplates were deposited at the liquid-air contact line. The solvent evaporated slowly over a 24-hour period at room temperature, leaving a uniform matte-gray film covering the substrate and vessel walls.

S^{2-} ligands were exchanged for oleylamine using a 21 mg/mL solution of Na_2S in methanol, which is a modification of the process reported by the Talapin group [18]. The Na_2S solution was dispensed on the nanoplate film and allowed to soak for 1 min, then was spun off at 3000 rpm for 30 s. To remove unbound OLA and S^{2-} ligands, two more spin-casting steps at 3000 rpm for 30 s were applied with chloroform and methanol.

2.2.3. Films from solution ligand exchange and electrophoretic deposition

After washing, $CuSbS_2$ nanoplates were dispersed in 10 mL of hexanes. Then 10 mL of Na_2S in formamide solution (21 mg/mL) was added slowly to the suspension, again adapting a literature procedure [18]. The less dense phase of nanoplates dispersed in hexanes separated to the top, while the Na_2S solution settled to the bottom of the centrifuge tube. The mixture was vortexed for 20 min to facilitate mixing and enable the S^{2-} to displace the OLA, rendering the nanoplates hydrophilic. The mixture was then left to phase separate for another 20 min, leaving the nanoplates dispersed in the polar formamide solvent. The hexanes were drawn off with a syringe and the electrostatically stabilized solution of $CuSbS_2$ nanoplates in formamide was washed by adding 10 mL of acetonitrile to cause flocculation of the particles. The particles were isolated by centrifugation at 6000 rpm for 5 min and redispersed in formamide. This process was repeated 3 times. After washing, the S^{2-}-capped $CuSbS_2$ nanoplates were dispersed in formamide and were stable for up to 5 days.

EPD was used to deposit mesoporous films of the $CuSbS_2$ nanoplates on conductive substrates. The EPD setup consisted of two electrodes separated by a 2.5 mm channel that was filled with a nanoplate dispersion of 9 mg/mL. S^{2-} capped nanoplates were deposited with a bias voltage of 5 V, while the oleylamine capped platelets were deposited at 250 V. In a typical deposition, the voltage was applied to two ITO ($Sn:In_2O_3$, Colorado Concept Coatings) electrodes for 20 min. The deposition solution was then withdrawn from the cell slowly with a syringe, leaving a matte gray film on the positive electrode.

2.3. Material characterization

Optical characterization of nanocrystal films was performed in diffuse reflectance geometry because the dimensions of the $CuSbS_2$ nanoplates render them highly scattering. UV/Vis/NIR spectroscopy was performed with a PE Lambda-950 spectrometer equipped with an integrating sphere (60 mm diameter, Labsphere, Inc). A Kubelka-Munk transformation and Tauc plot were used to calculate the absorbance spectrum and band gap of the $CuSbS_2$ films. Ligand exchange was evaluated using FTIR spectroscopy (Thermo-Scientific Nicolet iS 50R).

Film morphology and thickness were investigated by scanning electron microscopy (SEM, Zeiss Supra 50 VP). Crystallinity was evaluated by X-ray diffraction (XRD, Rigaku SmartLab) in grazing incidence mode for CBD films and in Bragg-Brentano mode for nanoplate films.

Transient photoconductivity in both dispersions and films of $CuSbS_2$ nanoplates was measured using time-resolved terahertz spectroscopy (TRTS) with a configuration described elsewhere [37]. Briefly, the output from a regeneratively amplified Ti:sapphire laser (Coherent Libra, 50 fs pulse duration, 800 nm wavelength, 1 kHz repetition rate) was split and directed to an optical parametric amplifier (Coherent OPerA Solo) to select the wavelength of the optical pump pulse and to ZnTe non-linear crystals to generate and detect terahertz radiation, with pump-probe delay time controlled by an optical delay line. The change in transmission or reflection of the terahertz electric field strength following photoexcitation was normalized by the non-photoexcited signal to determine $\Delta E/E_{ref}$. Nanoplate dispersions in hexanes were measured in a quartz cuvette with continuous stirring. Films were measured in transmission on quartz substrates, with the exception of EPD films which were measured in reflection on ITO substrates.

Phase Analysis Light Scattering (PALS) was used to measure the electrophoretic mobility of S^{2-}-capped $CuSbS_2$ nanoplates in formamide (Brookhaven NanoBrook Omni). PALS measurements were performed with a bias of 4 V alternating at 2 Hz.

3. Results and discussion

3.1. Films by CBD

Although direct solution deposition of the ternary compound $CuSbS_2$ as a conformal film is desirable, realization has been challenging. Synthesis of the chalcostibite phase by CBD requires fine control over concentrations of antimony and copper to avoid formation of binary impurities [9]. The binary compounds CuS and Sb_2S_3 have been readily grown by CBD in the literature; [34,35] however, reaction conditions are quite different due to different reaction kinetics and solubilities of the metal salts. CuS has been deposited at 70 °C.[19] However, such high temperatures would result in significant, undesirable precipitation for typical Sb_2S_3 recipes. Instead, Sb_2S_3 is typically grown at 4–10 °C to deposit uniform films on the substrate while

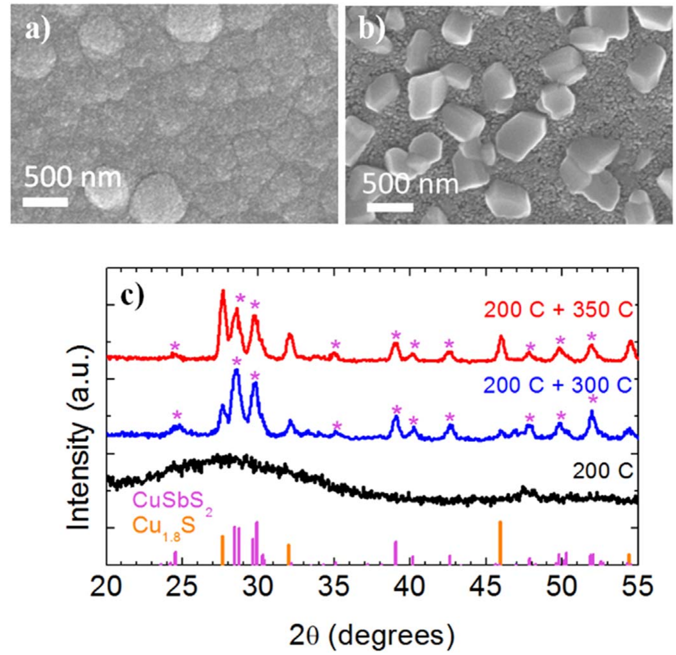

Fig. 1. SEM images of (a) as-grown CuS/Sb_2S_3 stacks on FTO substrate, and (b) film after annealing at 200 °C for 2 h, then 300 °C for 30 min. (c) XRD of films annealed under different conditions. *denotes peaks attributed to chalcostibite phase.

minimizing homogeneous nucleation [34,35]. Common CBD approaches to control free metal concentrations in solution employ ligands such as EDTA, citrate, and NTA that bind based on electronegativity of the metal cation [38,39], meaning that ligands preferentially complex with copper rather than antimony. Therefore it is difficult to find conditions where copper and antimony sulfides can be deposited with similar driving forces. Instead, the current state of the art for solution deposition is to sequentially deposit a bilayer of Cu/Sb by electrodeposition or mixed metal layer from hybrid inks and then sulfurize the metal stack [4,6].

We modified this bilayer strategy by depositing stacks of the binary compounds CuS and Sb_2S_3 and then using a two-stage annealing process to form ternary $CuSbS_2$. Fig. 1 shows SEM micrographs and XRD patterns for CuS/Sb_2S_3 stacks on FTO substrates, as-grown and after annealing in nitrogen at 200 °C for 2 h and then 300 °C for 30 min. The as-grown CuS/Sb_2S_3 stack was 400 nm thick, consisting of a 150 nm CuS layer and a 250 nm Sb_2S_3 layer, as measured by cross-sectional SEM (not shown). Bilayer thicknesses were chosen to match the desired $CuSbS_2$ stoichiometry. After annealing, the top-down SEM micrograph in Fig. 1b shows larger crystals on top of a floor layer. The floor layer is coarsened after annealing compared to the as-grown, likely because of species migration for crystal growth at energetically favorable sites. Thus, large crystals grow at the expense of small crystals in the floor layer, reducing uniformity. Chernomordik et al. have reported a similar phenomenon when annealing films of colloidal Cu_2ZnSnS_4 (CZTS) nanocrystals [40]. They also report reduction in the nanocrystal film thickness and increased formation of cracks as material from the nanocrystal layer is transported for growth of large grains [40].

XRD of the annealed CuS/Sb_2S_3 stacks, shown in Fig. 1c, indicates that chalcostibite crystallite size and phase purity depend on annealing temperature. Annealing at 200 °C enabled interdiffusion between layers, but did not result in formation of crystalline material. However, subsequent annealing at 300 °C resulted in crystallization and grain growth of the desired chalcostibite phase as well as the digenite ($Cu_{1.8}S$) impurity phase. Annealing at 350 °C resulted in sharpened chalcostibite peaks, indicating crystallite growth, but also resulted in an 85% increase in the integrated intensity of the digenite peak at 27.6°, presumably due to losses of the volatile Sb_2S_3 [3,41].

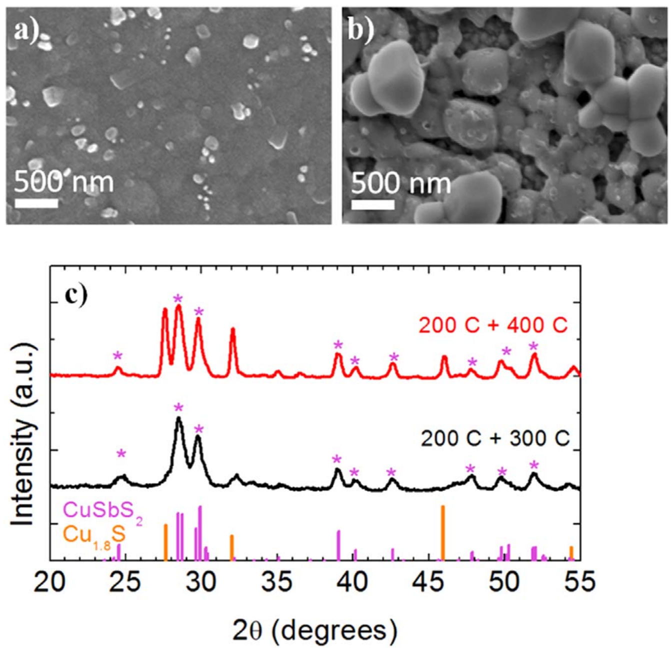

Fig. 2. SEM images of (a) $CuSbS_2$ films on FTO annealed at 200 °C for 2 h followed by 300 °C for 30 min in a glass enclosure with a 2.2 mm headspace, and (b) $CuSbS_2$ films on FTO annealed at 200 °C for 2 h followed by 400 °C for 30 min with a glass substrate resting directly on top of the film. (c) XRD patterns of the $CuSbS_2$ films in (a) and (b). *denotes peaks attributed to chalcostibite phase.

To suppress outgassing of volatile components, the overhead volume was reduced by enclosing the films with glass, allowing a saturation pressure of volatiles to be maintained in the headspace. Maintaining a 2.2 mm headspace resulted in formation of uniform films, Fig. 2a, and prevented $Cu_{1.8}S$ formation, Fig. 2c. However, larger grains on the order of the film thickness are desirable for use in a solar cell absorber layer. To increase grain size further, the crystal growth temperature was elevated to 400 °C. Even with the glass enclosure, at 400 °C the film outgassed significantly, and deposits on the roof of the glass enclosure were observed. Alternatively, stacks were annealed at 400 °C with a glass substrate in direct contact with the film, essentially reducing the overhead volume to zero. Under these conditions, the film formed large crystals with diameters of up to ~500 nm; however, large pinholes formed in the floor layer, Fig. 2b, and the digenite peak at 27.6° confirms the loss of phase purity. In CIGS, Na diffusion into the film from soda-lime glass substrates during annealing results in increased grain size [42]. However, use of Na-free substrates and enclosures such as a crystalline Si wafer did not affect the $CuSbS_2$ grain size. In an attempt to reduce outgassing of Sb_2S_3, the order of the binary stack was reversed, depositing the Sb_2S_3 film first followed by the CuS. However, this lead to preferential formation of the $Cu_{1.8}S$ phase due to the high stability of this phase relative to others in the Cu_xS phase space [34].

3.2. Films by deposition of colloidal nanocrystals

The second approach for film fabrication employed colloidal nanocrystal building blocks. $CuSbS_2$ nanoplates were synthesized via colloidal hot-injection as reported by Ramasamy and coworkers (see Experimental Methods) [36]. Nanoplates synthesized with 30-minute reaction time had characteristic size of 400 nm by 500 nm with a thickness of 50 nm, as measured by SEM, Fig. 3a. Nanoplates synthesized with 10-minute reaction time were smaller on average, with a broader distribution of sizes, Fig. 3b.

XRD of the dropcast film, Fig. 3c, confirmed that the nanoplates grown for 30 min are almost purely chalcostibite phase. The amount of the digenite impurity phase, identified by the peaks at 27.6°, 32.0°, and 46.0°, increased when reaction time was 10 min or less, as reported by Ramasamy [36]. The relative heights of the peaks between 28°–29° and 29.5°–30° change with deposition time. The XRD in Fig. 3c, shows exaggeration of the (111) and (020) planes in the 30 min films compared to the powder reference, which may be due to differences in nanocrystal shape and packing orientation. A Tauc plot generated by Kubelka-Munk transformation of the diffuse reflectance data taken for nanocrystals grown for 30 min, Fig. 3d, indicates a direct band gap of 1.58 eV, which is comparable to other reports in the literature for $CuSbS_2$ [35,41].

While dropcast films of as-synthesized nanoplates were sufficient for physical and optical characterization, they did not yield uniform or conductive films. Consequently, both solution and solid-state exchange methods were used to replace the insulating oleylamine ligands with sulfide, as shown in Scheme 1. One route utilized convective assembly, spin-casting, or drop casting of films followed by solid-state ligand exchange with Na_2S, as detailed in Experimental Methods. Convective assembly and spin-casting provided facile methods to fabricate films of uniform thickness for further characterization on arbitrary substrates. However, these techniques are slow or wasteful and not scalable. Alternatively, the second route utilized solution exchange of ligands followed by EPD of films, which can be done over very large areas and with high atom economy. Furthermore, as we show below, EPD provides selective deposition of the desired phase and exclusion of undesired impurities.

3.2.1. Films from convective assembly and solid-state ligand exchange

Dispersions of $CuSbS_2$ nanoplates in chloroform were fabricated into mesoporous films by convective assembly, where a substrate was immersed in a colloidal dispersion while the solvent was allowed to evaporate, forcing particles toward the liquid-air contact line. Fig. 4 shows the resulting uniform matte gray films over an area of 4 cm^2. The nanoplates formed disordered mesoporous films rather than packing into an ordered array as reported for systems of more geometrically symmetric and monodisperse particles [43–45]. Films thickness was approximately 10 μm for conditions described in the Experimental Methods. 10 μm is thicker than required for efficient light harvesting and likely to be too thick for efficient charge collection in solar cells [4]. Film thickness can be reduced by increasing the evaporation rate or reducing the nanoplate concentration. For example, increasing the bath temperature to 40 °C was found to decrease film thickness to 2.8 μm.

After deposition of the mesoporous film, oleylamine ligands were exchanged to S^{2-} to increase the electronic coupling between nanoplates. Ligand exchange is a two-step process that depends upon removal of one species followed by binding of the replacement [17] and requires that both ligand species are soluble in the ligand exchange solution. Finding appropriate solvent-ligand combinations to meet these constraints can be a significant challenge, and protocols developed for one materials system may not be transferrable to others. The most successful exchange procedure that we tested for $CuSbS_2$ entailed capping with S^{2-} in methanol solvent. FTIR was used to measure the efficacy of solid-state ligand exchange by monitoring the C—H stretching features at 2850, 2920, and 2960 cm^{-1} that come from the oleylamine ligand, as shown in Fig. 5a.

The C—H stretching features present in the as-grown nanoplate sample are reduced by 83% upon exchange of the oleylamine ligands, even with only 1 min of exchange time. The nanocrystals appeared to partially fuse together after ligand exchange, Fig. 5b, a phenomenon that has also been reported for other nanocrystal films such as $CsPbI_3$ [46]. Because of the large size of the nanoplates and small volume fraction of ligands, solid state ligand exchange did not result in cracking due to reduction in interparticle spacing, as observed in other nanocrystal systems [47]. XRD of the films confirmed that phase purity was retained.

We also tried several other ligand-solvent combinations, but with

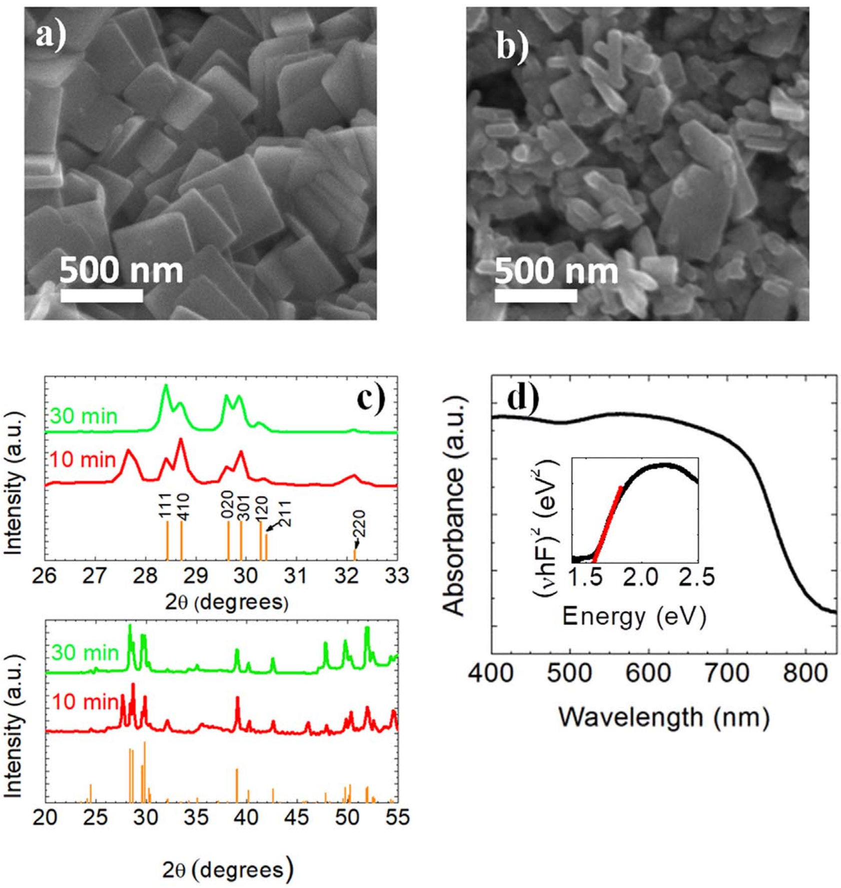

Fig. 3. SEM images of dropcast $CuSbS_2$ nanoplates synthesized for (a) 30 min and (b) 10 min. (c) XRD pattern of the same samples as in (a) and (b), shown over two ranges of diffraction angle. Reference spectrum for chalcostibite XRD (JCPDS 00-044-1417) shown as vertical orange lines. (d) Absorption spectrum of a $CuSbS_2$ nanoplate film similar to sample (a) measured by diffuse reflectance. Tauc plot in inset indicates a band gap of 1.58 eV.

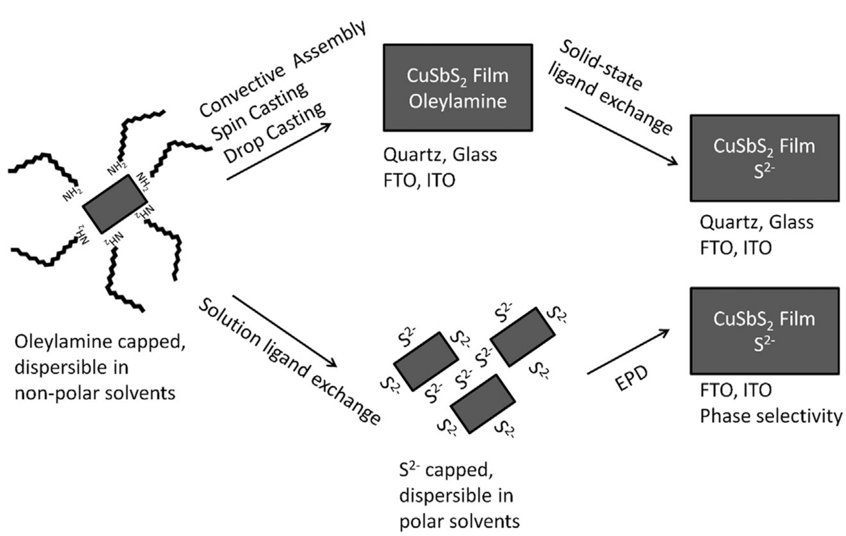

Scheme 1. Processing routes for fabrication of conductive, S^{2-} capped mesoporous films from dispersions of oleylamine-capped $CuSbS_2$ nanoplates.

less success. For example, exposing the nanoplates to S^{2-} in formamide did not result in the necessary removal of the original oleylamine ligands. FTIR in Fig. 5a shows < 25% reduction of the oleylamine peaks after 5 min of exchange time. Increasing the time to 20 min does not result in any further improvement. We posit that methanol is more effective because it is sufficiently hydrophobic to adequately solvate both the oleylamine and sulfide species. Exchange to SCN^- has also been employed to improve electronic coupling between nanocrystals, particularly with CdSe and PbSe. However we observed only minimal exchange of the original ligands when treating $CuSbS_2$ nanoplates with SCN^- in methanol, consistent with its milder reactivity compared to S_2^- [20,23].

The atomic S^{2-} ligand reduced the interparticle spacing and enhanced charge transfer compared to the insulating oleylamine. Four-point probe measurements of $CuSbS_2$ films fabricated via convective assembly showed that conductivity increased by two orders of magnitude upon ligand exchange from oleylamine (10^{-4} S/cm) to S^{2-} (10^{-2} S/cm). This increase in conductivity indicates that intercrystal contact resistance is quite significant for charge transport through the mesoporous film despite the relatively large 400 nm particle size and small number of contact points compared to quantum dot films. Charge transport is still possible even with the native oleylamine ligand, presumably due to incomplete ligand coverage on the surface of the nanoplates. Conductivities of ligand-exchanged films are comparable to

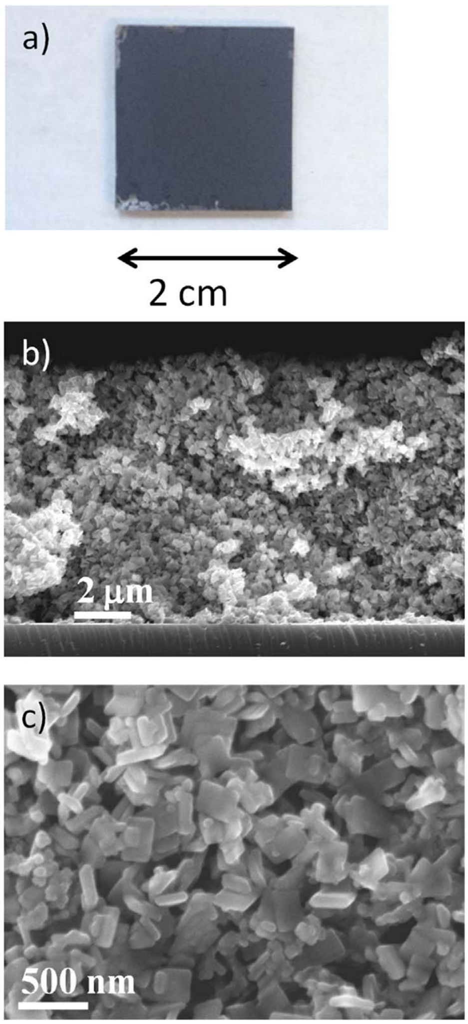

Fig. 4. (a) Photograph of a $CuSbS_2$ film on a glass substrate deposited by convective assembly from dispersions of $CuSbS_2$ in chloroform. $CuSbS_2$ synthesis time was 10 min. (b) Cross-sectional and (c) top-down SEM images of the film in (a).

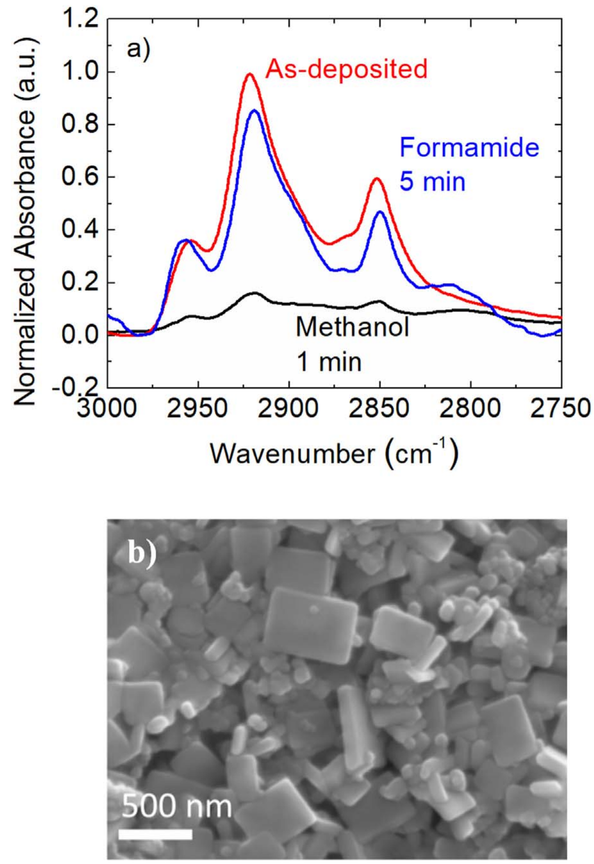

Fig. 5. (a) FTIR spectra of a $CuSbS_2$ film on a quartz substrate as-synthesized and after ligand exchange to S^{2-} in formamide and methanol. (b) SEM image of solid-state exchanged films of $CuSbS_2$ nanoplates. Nanoplate synthesis time was 10 min.

those reported for phase-pure $CuSbS_2$ deposited by co-sputtering of Sb_2S_3/Cu_2S by the Zakutayev group [41], although carrier concentrations and mobilities were not independently determined.

3.2.2. Films from solution ligand exchange and electrophoretic deposition

Ligand exchange in solution resulted in dispersions of S^{2-}-capped nanoplates that were electrostatically stabilized in polar formamide. Here the ligand exchange step was performed in a polar/non-polar biphasic solvent system, where the arriving (polar) and departing (non-polar) ligands are individually solubilized in their respective phases. These dispersions exhibited increased stability (5 days) compared to as-synthesized nanoplates in chloroform (2 days) or in hexanes (~4 h). Convective assembly and spin-casting could not be used to fabricate films from these dispersions due to the low vapor pressure of formamide, but the inks had excellent properties for EPD of films.

EPD is an inexpensive and scalable method for deposition of charged particles into films via electrophoresis in an electric field applied between two electrodes [48–50]. EPD offers the benefit of reduced deposition time and reduced waste compared to convective assembly and spin-casting. While EPD has been applied on a commercial scale to insulators and conductors since the 1940s, deposition of semiconductors presents a greater challenge because high applied voltages can damage the material [51]. Application of EPD to nanocrystal dispersions has been studied both in batch [52–54] and continuous reactors [55] for deposition of dense films [56]. In these works, the applied voltages are typically in the range of hundreds of volts. Here we show that ligand exchange can increase the surface charge and resulting electrophoretic mobility to reduce the voltage threshold for deposition to below 5 V.

As-synthesized nanoplates with oleylamine ligand had electrophoretic mobilities that were too small to reliably measure, and they required large voltages of at least 250 V that risk damaging the semiconductor nanocrystals. In contrast, uniform mesoporous films of S^{2-}-capped nanoplates in formamide could be deposited with applied bias of only 5 V, as shown in Fig. 6(a,b), because of their higher electrophoretic mobilities of $(-6 \pm 2) \times 10^{-9}$ m^2/V-s, as measured by dynamic light scattering.

As an additional advantage, EPD enabled selective deposition of the chalcostibite phase without the digenite phase. Nanoplates synthesized for 10 min that contain a mixture of both phases were deposited by EPD and convective assembly and characterized by SEM and XRD, Fig. 6. XRD of the EPD films confirms the absence of the $Cu_{1.8}S$ phase, while the convective assembly film clearly exhibits this digenite peaks at 27.6° and 32.1°, Fig. 6d. We speculate that the small particles that are visible only in the convective assembly films (and only in films made from the mixed phase colloids), Fig. 6c, are the digenite impurity phase. The selective deposition by EPD could be due to a combination of higher surface charge (i.e. greater electrophoretic mobility) and higher propensity toward sedimentation of the larger chalcostibite plates. Such considerations have been shown to influence the purification of nanocrystals by EPD previously [57].

3.3. Carrier dynamics

Photoexcited carrier lifetime and mobility determine the carrier

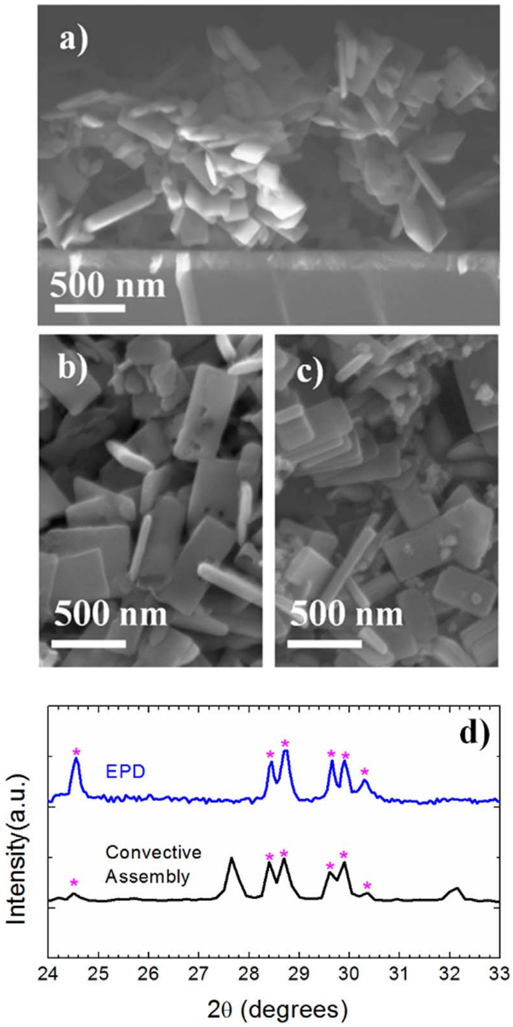

Fig. 6. (a) Cross-sectional and (b) top-down SEM images of EPD films of solution-exchanged $CuSbS_2$ nanoplates synthesized with a reaction time of 10 min. (c) Films deposited by convective assembly from the same batch of nanoplates used for (b). (d) XRD of films used in (b) and (c). * denotes chalcostibite phase peaks.

diffusion length, which is a key parameter in solar cell design. Additionally, carrier lifetime is a sensitive indicator of film quality and has been directly correlated to open circuit voltage in CdTe and CIGS devices [58,59]. Mobility and lifetime were recently reported for co-sputtered $CuSbS_2$ films [7]. Solution-deposited dense films have shown promising mobilities of 40–65 $cm^2 V^{-1} s^{-1}$ [12,60], but data on lifetimes were not reported.

We used time-resolved terahertz spectroscopy (TRTS) to measure the transient photoconductivity of dispersions of as-synthesized $CuSbS_2$ nanoplates in hexanes, nanoplate films fabricated by convective assembly with oleylamine and S^{2-} ligands, and films deposited by EPD. TRTS is a pump – probe method that measures the transient photoconductivity on picosecond to nanosecond time scales [37]. TRTS uses a non-contact AC probe of electrical conductivity, making it ideally suited to investigate nanocrystalline films. Fig. 7(a) shows the dynamic response of S^{2-} capped films and an oleylamine-capped colloidal dispersion. To quantify components of the decay, the convective assembly film and colloidal dispersion data were fit to a tri-exponential decay model, $\frac{\Delta E}{\Delta E_{max}} = \sum_{i=1}^{i=3} C_i \exp\left(-\frac{t}{\tau_i}\right)$, where $\frac{\Delta E}{\Delta E_{max}}$ is the normalized photoconductivity, τ_i are the characteristic decay time constants, and C_i are the weight fractions. The weight fractions were constrained to sum to unity, and the fitted data are shown in Fig. 7(b).

The photoconductivity of the oleylamine-capped nanoplate dispersion in hexane quickly decayed by 70% over tens of picoseconds, followed by a slower decay which resulted in non-zero photoconductivity even beyond 1 ns. The tri-exponential fit revealed time constants of 5.7 ± 0.6, 34 ± 4, and 1360 ± 270 ps with respective weight fractions of 0.54 ± 0.04, 0.42 ± 0.04, and 0.06 ± 0.006. The photoconductivity of the S^{2-}-capped nanoplate film decayed with nearly identical time constants to those of the olelyamine-capped dispersion, as shown in Table 1, although the weight fraction of the fastest component was larger at 0.72 ± 0.14.

The EPD film showed generally similar dynamics to the convective assembly film and the colloidal dispersion. The conductive ITO substrate needed for EPD does not transmit the terahertz probe. Reflection geometry enabled measurement of dynamics, although the combination of reflection geometry and the conductive substrate led to low signal-to-noise ratio [61]. While it is clear that dynamics proceed on the picosecond to nanosecond time scale, additional fitting was not attempted because of the large uncertainty.

Assuming constant mobility of untrapped photoexcited carriers, the dynamics of the photoconductivity are directly related to the decrease in density of photoexcited mobile carriers. Decay dynamics for the S^{2-}-capped convective assembly film were independent of pulse energy over 8–100 μJ/cm^2 and independent of pump wavelength over 400–700 nm, as shown in Fig. 7c and d. The independence with respect to carrier density indicates that higher order processes such as Auger and radiative recombination are not significant. Instead, the fast decay within the first ~100 ps is likely caused by trapping of photoexcited carriers, in agreement with previous suggestions for sputtered films [7]. The similar dynamics between S^{2-}-capped nanoplates and olelyamine-capped dispersions indicates that surface trapping is less important than bulk trapping, which is reasonable given the large particle size. However, in the S^{2-}-capped films the percentage of carriers trapped within 100 ps is slightly larger, likely due to increased number of surface defects in S^{2-}-capped film relative to the olyelamine-capped dispersion.

The longer time dynamics show that a small fraction of carriers, ~3% for oleylamine-capped dispersions and ~2% for the S^{2-}-capped film, have photoconductivities that persist for longer than 1 ns. Considering that photoexcitation is likely in the high-injection limit and given that dynamics are independent of pump fluence, this time scale may correspond to Shockley-Read-Hall recombination at bulk defects. Alternatively, the time scale may to de-trapping times, as has been observed for kesterites [62]. We note that the fraction of long-lived carriers and their lifetime are remarkably similar to those of co-sputtered $CuSbS_2$ films [7].

In addition to providing dynamics to evaluate trapping and recombination, TRTS also enables calculation of carrier mobility, μ, from the photoconductivity, σ, using Eq. 1

$$\sigma = e\mu n \tag{1}$$

where e is the elementary charge and n is the photoexcited carrier concentration. The photoconductivity of a thin film on a substrate can be calculated using Eq. 2 [63].

$$\sigma(t_p) = -\frac{\Delta E(t_p)}{E_{ref}} x \frac{2n_{eff} c\varepsilon_o}{d} \tag{2}$$

where n_{eff} is the refractive index of the mesoporous film, c is the speed of light, ε_0 is the permittivity of free space, d is the thickness of the photoexcited portion of the film, and t_p is the pump-probe delay time. Carrier mobilities of ~1 $cm^2 V^{-1} s^{-1}$ were found for the S^{2-}-capped nanoplate films, given that $|\Delta E(t_p = 0)/E_{ref}| = 0.011$ for pump fluence of 14 μJ/cm^2 and wavelength of 400 nm. Several approximations are implicit in this calculation. The refractive index of the mesoporous film was calculated using a simple linear effective medium approximation, $n_{eff} = (1\text{-}\varepsilon)\, n_{CuSbS2} + \varepsilon\, n_{air}$, where ε is the void fraction (estimated to be 0.50) and n_{CuSbS2} is 2.7 according to Reference [64]. For conductivity, d is estimated as the $1/e$ optical penetration depth, which we calculate to be 90 nm based on reported absorption coefficient data

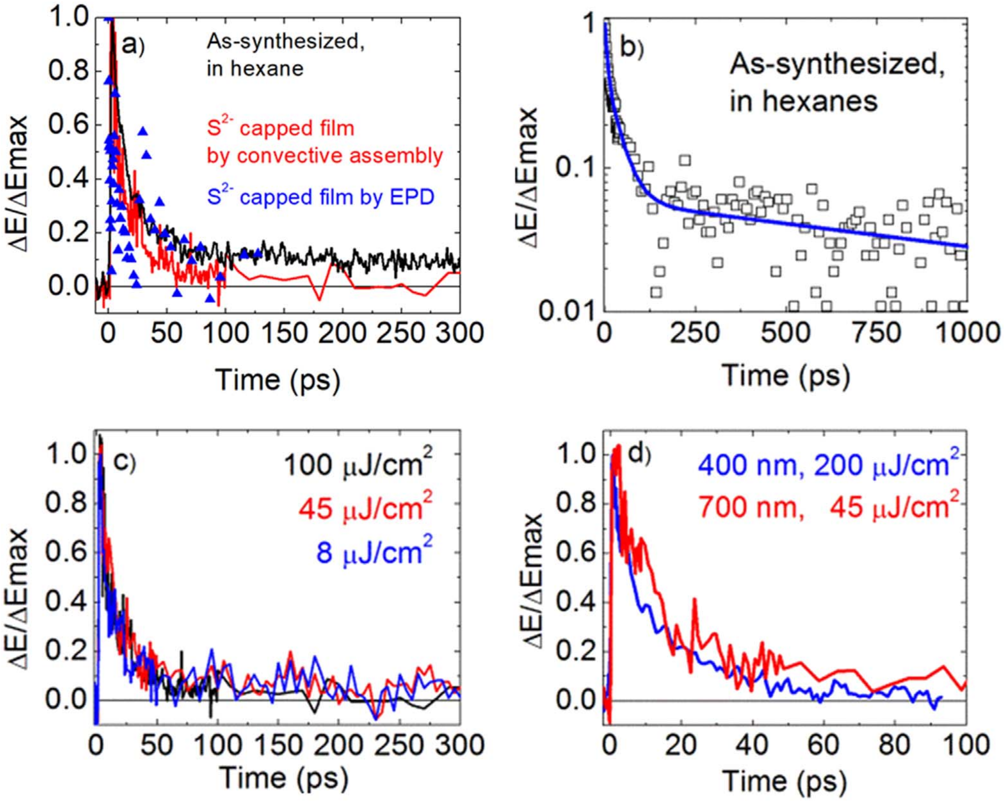

Fig. 7. (a) Normalized TRTS photoconductivity for a film of S^{2-}-capped $CuSbS_2$ nanoplates from convective assembly on quartz and a colloidal dispersion of as-synthesized, oleylamine-capped $CuSbS_2$ in hexanes. Both were pumped at 700 nm with 100 μJ/cm^2 and measured in transmission. EPD films measured in reflection and pumped at 400 nm are also shown. (b) Dynamic response of the as-synthesized $CuSbS_2$ in hexanes shown in (a) with a tri-exponential fit (blue line), shown on a log scale and over longer time range. (c) Normalized TRTS photoconductivity for a film of S^{2-} capped nanoplates on quartz pumped at 700 nm with several different pulse energies as indicated in the legend. (d) Normalized TRTS photoconductivity for the same film as in (c) pumped at 400 nm and 700 nm. (For interpretation of the references to color in this figure legend, the reader is referred to the web version of this article.)

Table 1
Best fit parameters of tri-exponential decay for data and fit shown in Fig. 7b and for that recorded from the S^{2-} capped film deposited by convective assembly (fit not shown).

	C_1	τ_1 (ps)	C_2	τ_2 (ps)	C_3	τ_3(ps)
S^{2-} film by convective assembly	0.72 ± 0.14	6.2 ± 1.3	0.32 ± 0.14	30 ± 14	0.03 ± 0.02	1800 ± 5400[a]
as-synthesized in hexanes	0.54 ± 0.04	5.7 ± 0.6	0.42 ± 0.04	34 ± 4	0.06 ± 0.01	1360 ± 270

[a] This parameter has a large uncertainty due to the very small signal (0.02) past 100 ps.

[7] at the pump wavelength of 400 nm, although factors of *d* cancel out in the calculation of mobility. The initial carrier density in $CuSbS_2$ was 4.4×10^{19} cm^{-3}, which assumes that every incident photon is absorbed within the penetration depth and generates both an electron and a hole that contribute equally to the conductivity. Matched electron and hole mobilities were previously reported for $CuSbS_2$ [7] and also predicted by theoretical calculations of similar effective masses [65,66]. Despite the numerous assumptions, the mobility of ~1 cm^2 V^{-1} s^{-1} in our mesoporous nanoplate films synthesized at 220 °C is consistent with the range of 2.5–4.1 cm^2 V^{-1} s^{-1} reported by the Zakutayev group for compact co-sputtered $CuSbS_2$ films under different annealing conditions up to 500 °C [7].

Comparison of the diffusion length and absorption depth provides a useful first indicator of the potential of a material for use as a photovoltaic absorber. Optimistic diffusion lengths of ~60 nm are estimated based on the mobility of ~1 cm^2 V^{-1} s^{-1} and a lifetime of 1.3 ns taken from the longest time constant in the model fit. The absorption coefficient for $CuSbS_2$ is 9×10^4 cm^{-1} at 1.8 eV [7], yielding an absorption depth of 110 nm. The small diffusion length relative to the absorption depth portends the possibility of poor carrier collection for wavelengths near the band edge, which is consistent with the decrease in external quantum efficiency between 650 and 750 nm reported by Septina et al. [4] However, CdS buffer layers reportedly form a cliff-like band offset with $CuSbS_2$, and selection of a more appropriate buffer layer may enable improved charge collection through the formation of more ideal space charge region.

4. Conclusion

Solution processing of $CuSbS_2$ for solar cell applications was investigated using CBD and colloidal nanocrystal synthesis and deposition. Conditions were not found for direct CBD of ternary chalcostibite. $CuSbS_2$ films could be fabricated by annealing binary CuS/Sb_2S_3 stacks in nitrogen atmosphere, but simultaneous control over the film morphology and phase purity was elusive. In contrast, phase-pure chalcostibite colloidal nanoplates with characteristic dimensions of 400 × 500 × 50 nm could be synthesized at temperatures of only 220 °C. As-synthesized nanoplates were capped with oleylamine ligands, which were replaced with S^{2-} to form functional mesoporous films using two different approaches: convective assembly followed by solid-state ligand exchange, and solution ligand exchange followed by electrophoretic deposition.

Characterization of the mesoporous films indicates some promise for $CuSbS_2$ as a thin film solar cell material, with band gap of 1.58 eV, mobilities of ~1 cm^2 V^{-1} s^{-1}, and transient photoconductivities exceeding 1 ns. Multiple pathways are possible to enhance the properties of films made from $CuSbS_2$ nanoplate building blocks. For example, other ligands such as mercaptopropionic acid that have been demonstrated to give optimal performance in quantum dot solar cells could be exchanged for oleylamine rather than S^{2-} [67]. Our previous studies of PbSe quantum dot films have indicated that S^{2-} ligands are desirable for enhanced mobility but result in shorter lifetimes than short organic ligands [23]. Alternatively, the nanoplate building blocks could be annealed in appropriate atmosphere to coalesce and densify the film while maintaining phase purity and control over defect types and densities. Annealing nanocrystals into compact films has proven to be an effective strategy for CZTSSe solar cells [68–70]. While more development is certainly needed, the work reported here indicates the potential to utilize high-quality $CuSbS_2$ nanoplate building blocks with scalable processing strategies for photovoltaic devices.

Acknowledgements

This work was supported by NSF CBET-1333649, NSF CMMI-1463412, NSF DMR-1507988, and made use of Drexel University's Core Facilities. M.E.E. was also partially supported by NSF GK-12 award DGE-0947936. We also acknowledge Rainer Eichberger and Hannes Hempel at Helmholtz Zentrum Berlin for assistance with measurement of TRTS in reflection geometry for EPD films.

References

[1] P. Jackson, R. Wuerz, D. Hariskos, E. Lotter, W. Witte, M. Powalla, Effects of heavy alkali elements in Cu(In,Ga)Se_2 solar cells with efficiencies up to 22.6%, Phys. Status Solidi Rapid Res. Lett. 10 (2016) 583–586, http://dx.doi.org/10.1002/pssr.201600199.

[2] W. Wang, M.T. Winkler, O. Gunawan, T. Gokmen, T.K. Todorov, Y. Zhu, D.B. Mitzi, Device characteristics of CZTSSe thin-film solar cells with 12.6% efficiency, Adv. Energy Mater. 4 (2014) 1301465, , http://dx.doi.org/10.1002/aenm.201301465.

[3] A. Zakutayev, L.L. Baranowski, A.W. Welch, C.A. Wolden, E.S. Toberer, Comparison of Cu_2SnS_3 and $CuSbS_2$ as potential solar cell absorbers, 40th Photovolt, Spec. Conf. 3 (2014) 2436–2438, http://dx.doi.org/10.1109/PVSC.2014.6925421.

[4] W. Septina, S. Ikeda, Y. Iga, T. Harada, M. Matsumura, Thin film solar cell based on $CuSbS_2$ absorber fabricated from an electrochemically deposited metal stack, Thin Solid Films 550 (2014) 700–704, http://dx.doi.org/10.1016/j.tsf.2013.11.046.

[5] A.W. Welch, L.L. Baranowski, P. Zawadzki, S. Lany, C.A. Wolden, A. Zakutayev, $CuSbSe_2$ photovoltaic devices with 3% efficiency, Appl. Phys. Express 8 (2015) 82301, , http://dx.doi.org/10.7567/APEX.8.082301.

[6] S. Banu, S.J. Ahn, S.K. Ahn, K. Yoon, A. Cho, Fabrication and characterization of cost-efficient $CuSbS_2$ thin film solar cells using hybrid inks, Sol. Energy Mater. Sol. Cells 151 (2016) 14–23, http://dx.doi.org/10.1016/j.solmat.2016.02.013.

[7] F.W. de S. Lucas, A.W. Welch, L.L. Baranowski, P.C. Dippo, H. Hempel, T. Unold, R. Eichberger, B. Blank, U. Rau, L.H. Mascaro, A. Zakutayev, Effects of thermochemical treatment on $CuSbS_2$ photovoltaic absorber quality and solar cell reproducibility, J. Phys. Chem. C 120 (2016) 18377–18385, http://dx.doi.org/10.1021/acs.jpcc.6b04206.

[8] S. Manolache, A. Duta, L. Isac, M. Nanu, A. Goossens, J. Schoonman, The influence of the precursor concentration on $CuSbS_2$ thin films deposited from aqueous solutions, Thin Solid Films 515 (2007) 5957–5960, http://dx.doi.org/10.1016/j.tsf.2006.12.046.

[9] B. Yang, L. Wang, J. Han, Y. Zhou, H. Song, S. Chen, J. Zhong, L. Lv, D. Niu, J. Tang, $CuSbS_2$ as a promising earth-abundant photovoltaic absorber material: a combined theoretical and experimental study, Chem. Mater. 26 (2014) 3135–3143, http://dx.doi.org/10.1021/cm500516v.

[10] A. Rabhi, M. Kanzari, B. Rezig, Optical and structural properties of $CuSbS_2$ thin films grown by thermal evaporation method, Thin Solid Films 517 (2009) 2477–2480, http://dx.doi.org/10.1016/j.tsf.2008.11.021.

[11] Y. Rodriguez-Lazcano, M.T.S. Nair, P.K. Nair, $CuSbS_2$ thin film formed through annealing chemically deposited Sb_2S_3-CuS thin films, J. Cryst. Growth 223 (2001) 399–406.

[12] C.L. McCarthy, P. Cottingham, K. Abuyen, E.C. Schueller, S.P. Culver, R.L. Brutchey, Earth abundant CuSbS $_2$ thin films solution processed from thiol–amine mixtures, J. Mater. Chem. C 4 (2016) 6230–6233, http://dx.doi.org/10.1039/C6TC02117D.

[13] S. Suehiro, K. Horita, M. Yuasa, T. Tanaka, K. Fujita, Y. Ishiwata, K. Shimanoe, T. Kida, Synthesis of copper-antimony-sulfide nanocrystals for solution-processed solar cells, Inorg. Chem. 54 (2015) 7840–7845, http://dx.doi.org/10.1021/acs.inorgchem.5b00858.

[14] C.R. Kagan, E. Lifshitz, E.H. Sargent, D.V. Talapin, Building devices from colloidal quantum dots, Science 353 (2016), http://dx.doi.org/10.1126/science.aac5523.

[15] M. Yuan, M. Liu, E.H. Sargent, Colloidal quantum dot solids for solution-processed solar cells, Nat. Energy. 1 (2016) 16016, , http://dx.doi.org/10.1038/nenergy.2016.16.

[16] C.-H.M. Chuang, P.R. Brown, V. Bulović, M.G. Bawendi, Improved performance and stability in quantum dot solar cells through band alignment engineering, Nat. Mater. 13 (2014) 1–6, http://dx.doi.org/10.1038/nmat3984.

[17] M.A. Boles, D. Ling, T. Hyeon, D.V. Talapin, The surface science of nanocrystals, Nat. Mater. 15 (2016) 141–153, http://dx.doi.org/10.1038/nmat4526.

[18] A. Nag, M.V. Kovalenko, J.-S. Lee, W. Liu, B. Spokoyny, D.V. Talapin, Metal-free inorganic ligands for colloidal nanocrystals: S^{2-}, HS^-, Se^{2-}, HSe^-, Te^{2-}, HTe^-, TeS_3^{2-}, OH^-, and NH^{2-} as surface ligands, Anal. Chem. 133 (2011) 10612–10620, http://dx.doi.org/10.1021/ja2029415.

[19] M.V. Kovalenko, M. Scheele, D.V. Talapin, Colloidal nanocrystals with molecular metal chalcogenide surface ligands, Science 324 (2009) 1417–1420, http://dx.doi.org/10.1126/science.1170524.

[20] A.T. Fafarman, W.K. Koh, B.T. Diroll, D.K. Kim, D.K. Ko, S.J. Oh, X. Ye, V. Doan-Nguyen, M.R. Crump, D.C. Reifsnyder, C.B. Murray, C.R. Kagan, Thiocyanate-capped nanocrystal colloids: vibrational reporter of surface chemistry and solution-based route to enhanced coupling in nanocrystal solids, J. Am. Chem. Soc. 133 (2011) 15753–15761, http://dx.doi.org/10.1021/ja206303g.

[21] R.P. Andres, J.D. Bielefeld, J.I. Henderson, D.B. Janes, V.R. Kolagunta, C.P. Kubiak, W.J. Mahoney, R.G. Osifchin, Self-assembly of a two-dimensional superlattice of molecularly linked metal clusters, Science 273 (1996) 1690–1693, http://dx.doi.org/10.1126/science.273.5282.1690.

[22] D. Yu, C. Wang, P. Guyot-Sionnest, n-Type conducting CdSe nanocrystal solids, Science 300 (2003) 1277–1280, http://dx.doi.org/10.1126/science.1084424.

[23] G.W. Guglietta, B.T. Diroll, E.A. Gaulding, J.L. Fordham, S. Li, C.B. Murray, J.B. Baxter, Lifetime, mobility, and diffusion of photoexcited carriers in ligand-exchanged lead selenide nanocrystal films measured by time-resolved terahertz spectroscopy, ACS Nano 9 (2015) 1820–1828, http://dx.doi.org/10.1021/nn506724h.

[24] E.D. Goodwin, B.T. Diroll, S.J. Oh, T. Paik, C.B. Murray, C.R. Kagan, Effects of post-synthesis processing on CdSe nanocrystals and their solids: correlation between surface chemistry and optoelectronic properties, J. Phys. Chem. C 118 (2014) 27097–27105, http://dx.doi.org/10.1021/jp5076912.

[25] J.-S. Lee, M.V. Kovalenko, J. Huang, D.S. Chung, D.V. Talapin, Band-like transport, high electron mobility and high photoconductivity in all-inorganic nanocrystal arrays, Nat. Nanotechnol. 6 (2011) 348–352, http://dx.doi.org/10.1038/nnano.2011.46.

[26] J. Tang, K.W. Kemp, S. Hoogland, K.S. Jeong, H. Liu, L. Levina, M. Furukawa, X. Wang, R. Debnath, D. Cha, K.W. Chou, A. Fischer, A. Amassian, J.B. Asbury, E.H. Sargent, Colloidal-quantum-dot photovoltaics using atomic-ligand passivation, Nat. Mater. 10 (2011) 765–771, http://dx.doi.org/10.1038/nmat3118.

[27] E.L. Rosen, R. Buonsanti, A. Llordes, A.M. Sawvel, D.J. Milliron, B.A. Helms, Exceptionally mild reactive stripping of native ligands from nanocrystal surfaces by using Meerwein's salt, Angew. Chem. Int. Ed. 51 (2012) 684–689, http://dx.doi.org/10.1002/anie.201105996.

[28] E. Talgorn, Y. Gao, M. Aerts, L.T. Kunneman, J.M. Schins, T.J. Savenije, M.a. van Huis, H.S.J. van der Zant, A.J. Houtepen, L.D.a. Siebbeles, Unity quantum yield of photogenerated charges and band-like transport in quantum-dot solids, Nat. Nanotechnol. 6 (2011) 733–739, http://dx.doi.org/10.1038/nnano.2011.159.

[29] Z.M. Norman, N.C. Anderson, J.S. Owen, Electrical transport and grain growth in solution-cast, chloride-terminated cadmium selenide nanocrystal thin films, ACS Nano 8 (2014) 7513–7521, http://dx.doi.org/10.1021/nn502829s.

[30] J.J. Choi, J. Luria, B.R. Hyun, A.C. Bartnik, L. Sun, Y.F. Lim, J.A. Marohn, F.W. Wise, T. Hanrath, Photogenerated exciton dissociation in highly coupled lead salt nanocrystal assemblies, Nano Lett. 10 (2010) 1805–1811, http://dx.doi.org/10.1021/nl100498e.

[31] G.H. Carey, A.L. Abdelhady, Z. Ning, S.M. Thon, O.M. Bakr, E.H. Sargent, Colloidal Quantum Dot Solar Cells, Chem. Rev. 115 (2015) 12732–12763, http://dx.doi.org/10.1021/acs.chemrev.5b00063.

[32] K. Ramasamy, H. Sims, W.H. Butler, A. Gupta, Mono-, few-, and multiple layers of copper antimony sulfide ($CuSbS_2$): a ternary layered sulfide, J. Am. Chem. Soc. 136 (2014) 1587–1598, http://dx.doi.org/10.1021/ja411748g.

[33] Q. Liang, K. Huang, X. Ren, W. Zhang, R. Xie, S. Feng, Synthesis of Cu–Sb–S nanocrystals: insight into the mechanism of composition and crystal phase selection, CrystEngComm 18 (2016) 3703–3710, http://dx.doi.org/10.1039/C6CE00474A.

[34] C.S. Kim, S.H. Choi, J.H. Bang, New insight into copper sulfide electrocatalysts for quantum dot-sensitized solar cells: composition-dependent electrocatalytic activity and stability, ACS Appl. Mater. Interfaces 6 (2014) 22078–22087, http://dx.doi.org/10.1021/am505473d.

[35] S. Messina, M. Nair, P. Nair, Antimony sulfide thin films in chemically deposited thin film photovoltaic cells, Thin Solid Films 515 (2007) 5777–5782, http://dx.doi.org/10.1016/j.tsf.2006.12.155.

[36] K. Ramasamy, H. Sims, W.H. Butler, A. Gupta, Mono-, few-, and multiple layers of copper antimony sulfide ($CuSbS_2$): a ternary layered sulfide, J. Am. Chem. Soc. 136 (2014) 1587–1598, http://dx.doi.org/10.1021/ja411748g.

[37] J.B. Baxter, G.W. Guglietta, Terahertz spectroscopy, Anal. Chem. 83 (2011) 4342–4368, http://dx.doi.org/10.1021/ac200907z.

[38] B. Opasanont, J.B. Baxter, Dynamic speciation modeling to guide selection of complexing agents for chemical bath deposition: case study for ZnS thin films, Cryst. Growth Des. 15 (2015) 4893–4900, http://dx.doi.org/10.1021/acs.cgd.5b00789.

[39] G. Hodes, Chemical Solution Deposition of Semiconductor Films, CRC Press, Boca Raton, FL, 2002.

[40] B.D. Chernomordik, A.E. Béland, D.D. Deng, L.F. Francis, E.S. Aydil, Microstructure evolution and crystal growth in Cu_2ZnSnS_4 thin films formed by annealing colloidal nanocrystal coatings, Chem. Mater. 26 (2014) 3191–3201, http://dx.doi.org/10.1021/cm500791a.

[41] A.W. Welch, P.P. Zawadzki, S. Lany, C.A. Wolden, A. Zakutayev, Self-regulated growth and tunable properties of $CuSbS_2$ solar absorbers, Sol. Energy Mater. Sol. Cells 132 (2015) 499–506, http://dx.doi.org/10.1016/j.solmat.2014.09.041.

[42] D. Braunger, D. Hariskos, G. Bilger, U. Rau, H.W. Schock, Influence of sodium on the growth of polycrystalline Cu(In,Ga)Se_2 thin films, Thin Solid Films 361 (2000) 161–166, http://dx.doi.org/10.1016/S0040-6090(99)00777-4.

[43] Z. Chen, J. Moore, G. Radtke, H. Sirringhaus, S. O'Brien, Binary nanoparticle Superlattices in the semiconductor − semiconductor system: CdTe and CdSe, J. Am. Chem. Soc. 129 (2007) 15702–15709, http://dx.doi.org/10.1021/ja076698z.

[44] E.V. Shevchenko, D.V. Talapin, N.A. Kotov, S. O'Brien, C.B. Murray, Structural diversity in binary nanoparticle superlattices, Nature 439 (2006) 55–59, http://dx.

doi.org/10.1038/nature04414.
[45] C.B. Murray, C.R. Kagan, M.G. Bawendi, Self-organization of CdSe nanocrystallites into three-dimensional quantum dot superlattices, Science 270 (1995) 1335–1338, http://dx.doi.org/10.1126/science.270.5240.1335.
[46] S. Dastidar, D.A. Egger, L.Z. Tan, S.B. Cromer, A.D. Dillon, S. Liu, L. Kronik, A.M. Rappe, A.T. Fafarman, High chloride doping levels stabilize the perovskite phase of cesium lead iodide, Nano Lett. 16 (2016) 3563–3570, http://dx.doi.org/10.1021/acs.nanolett.6b00635.
[47] J.M. Luther, M. Law, Q. Song, C.L. Perkins, M.C. Beard, A.J. Nozik, Structural, optical, and electrical properties of self-assembled films of PbSe nanocrystals treated with 1,2-ethanedithiol, ACS Nano 2 (2008) 271–280, http://dx.doi.org/10.1021/nn7003348.
[48] A.R. Boccaccini, I. Zhitomirsky, Application of electrophoretic and electrolytic deposition techniques in ceramics processing, InterCeram Int. Ceram. Rev. 54 (2005) 242–246, http://dx.doi.org/10.1016/S1359-0286(02)00080-3.
[49] I. Corni, M.P. Ryan, A.R. Boccaccini, Electrophoretic deposition: from traditional ceramics to nanotechnology, J. Eur. Ceram. Soc. 28 (2008) 1353–1367, http://dx.doi.org/10.1016/j.jeurceramsoc.2007.12.011.
[50] O.O. Van der Biest, L.J. Vandeperre, Electrophoretic Deposition, Annu. Rev. Mater. Sci. 29 (1999) 327–352, http://dx.doi.org/10.1146/annurev.matsci.29.1.327.
[51] L. Besra, M. Liu, A review on fundamentals and applications of electrophoretic deposition (EPD), Prog. Mater. Sci. 52 (2007) 1–61, http://dx.doi.org/10.1016/j.pmatsci.2006.07.001.
[52] R. Mainz, A. Singh, S. Levcenko, M. Klaus, C. Genzel, K.M. Ryan, T. Unold, Phase-transition-driven growth of compound semiconductor crystals from ordered metastable nanorods, Nat. Commun. 5 (2014) 3133, , http://dx.doi.org/10.1038/ncomms4133.
[53] A. Singh, N.J. English, K.M. Ryan, Highly ordered nanorod assemblies extending over device scale areas and in controlled multilayers by electrophoretic deposition, J. Phys. Chem. B 117 (2013) 1608–1615, http://dx.doi.org/10.1021/jp305184n.
[54] K. Kornhuber, J. Kavalakkatt, X. Lin, A. Ennaoui, M.C. Lux-Steiner, In situ monitoring of electrophoretic deposition of Cu2ZnSnS4 nanocrystals, RSC Adv. 3 (2013) 5845, http://dx.doi.org/10.1039/c3ra23093g.
[55] A.D. Dillon, L. Le Quoc, M. Goktas, B. Opasanont, S. Dastidar, S. Mengel, J.B. Baxter, A.T. Fafarman, Thin films of copper indium selenide fabricated with high atom economy by electrophoretic deposition of nanocrystals under flow, Chem. Eng. Sci. 154 (2016) 128–135, http://dx.doi.org/10.1016/j.ces.2016.06.056.
[56] J.H. Dickerson, A.R. Boccaccini, Electrophoretic Deposition of Nanomaterials, Springer Science and Business Media LLC, New York, NY, 2012.
[57] J.D. Bass, X. Ai, A. Bagabas, P.M. Rice, T. Topuria, J.C. Scott, F.H. Alharbi, H.C. Kim, Q. Song, R.D. Miller, An efficient and low-cost method for the purification of colloidal nanoparticles, Angew. Chem. Int. Ed. 50 (2011) 6538–6542, http://dx.doi.org/10.1002/anie.201100112.
[58] W.K. Metzger, D. Albin, D. Levi, P. Sheldon, X. Li, B.M. Keyes, R.K. Ahrenkiel, Time-resolved photoluminescence studies of CdTe solar cells, J. Appl. Phys. 94 (2003) 3549–3555, http://dx.doi.org/10.1063/1.1597974.
[59] B. Ohnesorge, R. Weigand, G. Bacher, A. Forchel, W. Riedl, F.H. Karg, Minority-carrier lifetime and efficiency of Cu(In,Ga)Se_2 solar cells, Appl. Phys. Lett. 73 (1998) 1224–1226, http://dx.doi.org/10.1063/1.122134.
[60] B. Yang, L. Wang, J. Han, Y. Zhou, H. Song, S. Chen, J. Zhong, L. Lv, D. Niu, J. Tang, $CuSbS_2$ as a Promising Earth-Abundant Photovoltaic Absorber Material: A Combined Theoretical and Experimental Study, (2014).
[61] H. Hempel, T. Unold, R. Eichberger, Measurement of charge carrier mobilities in thin films on metal substrates by reflection time resolved terahertz spectroscopy, Opt. Express 25 (2017) 17227, , http://dx.doi.org/10.1364/OE.25.017227.
[62] C.J. Hages, A. Redinger, S. Levcenko, H. Hempel, M.J. Koeper, R. Agrawal, D. Greiner, C.A. Kaufmann, T. Unold, Identifying the real minority carrier lifetime in nonideal semiconductors: a case study of kesterite materials, Adv. Energy Mater. 7 (2017) 1700167, , http://dx.doi.org/10.1002/aenm.201700167.
[63] J.E. Murphy, M.C. Beard, A.J. Nozik, Time-resolved photoconductivity of PbSe nanocrystal arrays, J. Phys. Chem. B 110 (2006) 25455–25461, http://dx.doi.org/10.1021/jp0646123.
[64] Y. Fadhli, A. Rabhi, M. Kanzari, Effect of annealing time and substrates nature on the physical properties of $CuSbS_2$ thin films, J. Mater. Sci. Mater. Electron. 25 (2014) 4767–4773, http://dx.doi.org/10.1007/s10854-014-2231-5.
[65] S. Lany, Band-structure calculations for the 3d transition metal oxides in GW, Phys. Rev. B - Condens. Matter Mater. Phys. 87 (2013) 85112, http://dx.doi.org/10.1103/PhysRevB.87.085112.
[66] S. Lany, Semiconducting transition metal oxides, J. Phys. Condens. Matter 27 (2015) 283203, http://dx.doi.org/10.1088/0953-8984/27/28/283203.
[67] K.S. Jeong, J. Tang, H. Liu, J. Kim, A.W. Schaefer, K. Kemp, L. Levina, X. Wang, S. Hoogland, R. Debnath, L. Brzozowski, E.H. Sargent, J.B. Asbury, Enhanced mobility-lifetime products in PbS colloidal quantum dot photovoltaics, ACS Nano 6 (2012) 89–99, http://dx.doi.org/10.1021/nn2039164.
[68] Y. Cao, M.S. Denny, J.V. Caspar, W.E. Farneth, Q. Guo, A.S. Ionkin, L.K. Johnson, M. Lu, I. Malajovich, D. Radu, H.D. Rosenfeld, K.R. Choudhury, W. Wu, High-efficiency solution-processed $Cu_2ZnSn(S,Se)_4$ thin-film solar cells prepared from binary and ternary nanoparticles, J. Am. Chem. Soc. 134 (2012) 15644–15647, http://dx.doi.org/10.1021/ja3057985.
[69] C.J. Hages, M.J. Koeper, C.K. Miskin, K.W. Brew, R. Agrawal, Controlled grain growth for high performance nanoparticle-based Kesterite solar cells, Chem. Mater. 28 (2016) 7703–7714, http://dx.doi.org/10.1021/acs.chemmater.6b02733.
[70] Q. Guo, G.M. Ford, R. Agrawal, H.W. Hillhouse, Ink formulation and low-temperature incorporation of sodium to yield 12% efficient Cu(In,Ga)$(S,Se)_2$ solar cells from sulfide nanocrystal inks, Prog. Photovolt. Res. Appl. 21 (2013) 64–71, http://dx.doi.org/10.1002/pip.2200.